

Structural, microstructural and Mössbauer studies of nanocrystalline Fe_{100-x}Al_x powders elaborated by mechanical alloying

N. Boukherroub ^{a 1}, A. Guittoum ², N. Souami ², K. Akkouche ¹, S. Boutarfaia ³

¹LMMC, M'hamed Bougara University, Boumerdes, 35000, Algeria

²Nuclear Research Center of Algiers, 2 Bd Frantz Fanon, BP 399 Alger-Gare, Algiers, Algeria

³Nuclear Research Centre of Draria, BP 43, Algiers, Algeria

Abstract. Nanocrystalline Fe_{100-x}Al_x powders (x= 25, 30, 34 and 40 at %) were prepared by the mechanical alloying process using a vario-planetary high-energy ball mill for a milling time of 35 h. The formation and physical properties of the alloys were investigated as a function of Al content by means of X-ray diffraction, scanning electron microscopy (SEM), energy dispersive X-ray and Mössbauer spectroscopy. For all Fe_{100-x}Al_x samples, the complete formation of bcc phase was observed after 35 h of milling. As Al content increases, the lattice parameter increases, whereas the grain size decreases from 106 to 12 nm. The powder particle morphology for different compositions was observed by SEM. The Mössbauer spectra were adjusted with a singlet line and a sextet containing two components. The singlet was attributed to the formation of paramagnetic A2 disordered structure rich with Al. About the sextet, the first component indicated the formation of Fe clusters/ Fe-rich phases; however, the second component is characteristic of disordered ferromagnetic phase.

Keywords: Fe_{100-x}Al_x alloy; nanostructured powders; X-ray diffraction; microscopy; Mössbauer effect;

1 Introduction

Nanostructured materials have a crystallite size of the order of a few nanometres in at least one dimension [1]. Due to the extremely small size of the grains, a large fraction of the atoms in these materials is located at the grain boundaries and thus the material might exhibit unusual physical properties, compared to those of more conventional materials with microcrystalline grain size [2, 3].

Nanocrystalline Fe-based alloys combine the advantageous properties of various soft magnetic materials, such as high saturation induction and high permeability [4, 5]. The key of this property combination is the structural correlation length which is much smaller than the ferromagnetic one.

Among Fe-based compounds, Iron-aluminium alloys have drawn the attention of a large number of materials scientists for at least past four decades [6]. With the variation of composition, a series of binary FeAl alloys having different soft magnetic and physical properties can be obtained [7, 8]. Moreover, the relative simplicity of FeAl alloys in both the composition and structure (up to 70 at. %

^a e-mail : nadia.boukherroub@yahoo.fr

Al) and their and magnetic properties are up to date an object of numerous experimental and theoretical investigations [9].

Mechanical alloying (MA) is a powerful technique which allows the preparation of nanostructured FeAl alloys [10, 11]. It is an intensive energy process of mechanical grinding for the preparation of alloyed powders or composites in powder form [12]. It involves a repeated fracturing and welding of particles, leading to size reduction and particle shape changes [13].

Many works have been reported on the synthesis of FeAl alloys by different kinds of planetary ball mill systems (Low-energy horizontal [14, 15], SPEX 8000D [16, 17, 19, 20], High-energy planetary [18, 21]); however, to our knowledge, no reports on the elaboration of FeAl compounds by using the vario-planetary high energy ball mill (Fritsch P4) have been found in the literature. It is known that the high energy planetary ball mill (Fritsch P4) exhibits the particularity to control separately the rotation speeds of the main disk (ω) and the vials (Ω) and consequently the milling mode. We use the shock mode when $\Omega \gg \omega$ and the friction mode when $\Omega \ll \omega$ [22]. The effect of milling modes (friction or shock) has already been studied for $\text{Fe}_{80}\text{Ni}_{20}$ and $\text{Fe}_{90}\text{Ni}_{10}$ compounds [23] and it has been shown that the variation of milling mode influences the structural, hyperfine and magnetic properties of these alloys. In this perspective, we have studied the effect of Al content on the structural, microstructural and hyperfine properties of $\text{Fe}_{100-x}\text{Al}_x$ powder using the P4 planetary ball mill. To do so, we used two different values of Ω and ω . X-ray diffraction (XRD) and Mössbauer studies are used for a better understanding of the evolution of $\text{Fe}_{100-x}\text{Al}_x$ structure as a function of Aluminium content. Scanning electron microscopy (SEM) and X-ray microanalysis are also used to study the morphology of the powder and to investigate the chemical homogeneity of the powder particles.

2 Experiments

Elemental Fe and Al powders of 99.995 % purity and particle sizes of 50 μm and 4 μm respectively were separately weighted and mixed to get the desired composition. The mechanical alloying process was performed in a vario-planetary high-energy ball mill (Fritsch P4). The rotation speed of the disc, Ω , and the vials, ω , were equal to 150 rpm and 250 rpm respectively. To prevent oxidation phenomena, the mixed powder was sealed in a cylindrical vial under argon atmosphere with stainless steel balls. The ball-to-powder weight ratio was 30:1. To avoid excessive heating during milling, each 15 min of milling was followed by a pause of 15 min under Ar atmosphere. We have elaborated a series of $\text{Fe}_{100-x}\text{Al}_x$ sample with Al content of 25, 30, 34 and 40 (at %) for a fixed milling time of 35 h. XRD experiments were performed with a Philips X-Pert Pro diffractometer in continuous scanning mode using $\text{Cu K}\alpha$ radiation.

The X-ray patterns were analyzed by X'Pert High Score [24]. Each peak was fitted by a Pseudo-Voigt (PV) function in order to get the exact values of the interreticular spacing and the peaks broadening. The mean crystallite size and the mean level of microdistorsions (estimated by the Williamson–Hall method [25]) as well as the lattice parameter were calculated from the XRD data taking into account $\text{Cu K}\alpha_1$ radiation, after $\text{K}\alpha_2$ stripping using the Rachinger method. The instrumental broadening was determined using a Si standard (provided with the diffractometer) and subtracted from the experimental breadth to obtain the “pure” broadening of each diffraction line, which was then used for the Williamson–Hall calculations.

SEM and X-ray microanalysis studies were performed on a Philips XL 30 microscope coupled to an energy dispersive analyzer (EDX). Mössbauer spectra were obtained at room temperature with a Wissel instrument in the constant acceleration mode, using a radioactive ^{57}Co source diffused into a Rhodium matrix. Metallic iron was used for energy calibration and also as a reference for isomer shift. Mössbauer spectra were evaluated with the Recoil software using the Voigt-based hyperfine field distribution method (HFD-VB-F) [26].

3 Results and discussion

3.1 Structure

Fig. 1 shows the evolution of XRD patterns for $\text{Fe}_{100-x}\text{Al}_x$ ($x=25, 30, 34$ and 40 at %) samples as a function of Al content. XRD spectrum for the starting powder (labelled 0 h in Fig. 1) shows the reflections corresponding to distinct bcc Fe and fcc Al metals. This spectrum also shows that the Al (111) peak is the most intense and Al (200), (220), (222) and (400) peaks overlap with Fe (110), (200), (211) and (220) peaks respectively. After 35 h of milling, we observed that the Al peaks disappear completely, whereas the peaks related to Fe slightly shift towards lower angles. This proves that Al atoms dissolve in the Fe lattice leading to the formation of bcc solid solution (Fe–Al). The slightly angular shift is attributed to the formation of (Fe–Al) solid solution and also to the first-order internal stress induced by milling. The first-order of angular stress acts as a macroscopic level by modifying the lattice parameter and consequently produces an angular shift of XRD peaks [27]. Also, we can clearly observed that the diffraction peaks broaden after 35 h of milling for all X-ray peaks indicating a continuous decreases in the grain sizes and the introduction of lattice strain. This broadening is due to the second-order internal stress which acts at a macroscopic level of the crystallites and produces a broadening of X-ray peaks [27].

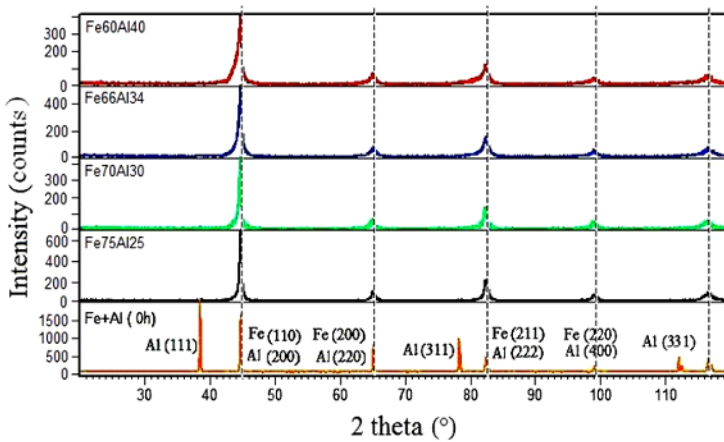


Fig. 1. X-ray diffraction spectra for $\text{Fe}_{100-x}\text{Al}_x$ powder after 35 h of milling time.

It is worth noting that for $\text{Fe}_{100-x}\text{Al}_x$ obtained by mechanical alloying, the formation of bcc solid solution Fe(Al) was confirmed by several authors. Indeed, E. Jartych et al. [28] showed the formation of bcc solid solution in $\text{Fe}_{100-x}\text{Al}_x$ (50, 60 and 70 at %) after 800 h using a conventional horizontal low energy ball mill. With a high energy ball mill (SPEX 8000M), V. Sebastian et al. [29] observed the total formation of bcc solid solution after 10 h of milling for $\text{Fe}_{100-x}\text{Al}_x$ ($x = 20, 40$ at %), while for ($x= 66, 80$ and 90 at %) the complete alloying was not achieved. Using a high energy ball mill (SPEX 8000D), the formation of bcc solid solution in $\text{Fe}_{100-x}\text{Al}_x$ for $x= 60$ and 65 at % has been confirmed by M. Krasnowski et al. [19] after 10 h and 15 h of milling respectively.

Fig. 2 shows the change of the lattice parameter, a (nm), versus Al content for $\text{Fe}_{100-x}\text{Al}_x$ ($x=25, 30, 34$ and 40 at %) samples after 35 h of milling. The lattice parameter increases slightly with Al content, from 0.28601 ± 0.00001 nm for pure Fe to 0.28609 ± 0.00001 , 0.28615 ± 0.00001 , 0.28645 ± 0.00001 , 0.28706 ± 0.00001 nm for 25, 30, 34 and 40 at % respectively. A similar behavior of a (nm) versus Al content (at %) was reported by E. Jartych et al. [30] for $\text{Fe}_{50}\text{Al}_{50}$, $\text{Fe}_{60}\text{Al}_{40}$ and $\text{Fe}_{70}\text{Al}_{30}$ nanostructure powders obtained after 800 h of milling using a conventional horizontal low

energy ball mill. The increases of a (nm) with Al (at %) is due to the larger atomic size of the Al atom ($r_{\text{Al}} = 0.143$ nm) in comparison with the Fe atom ($r_{\text{Fe}} = 0.124$ nm) [30].

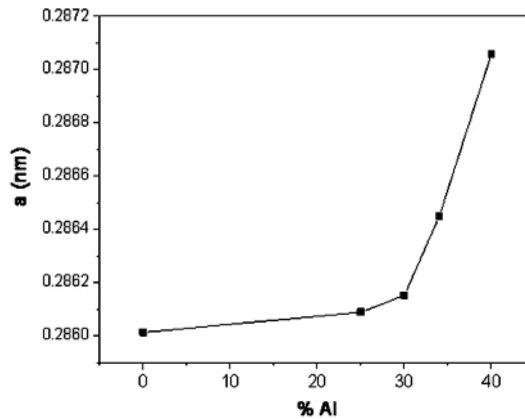


Fig. 2. Lattice parameter, a (nm), versus Al content for $\text{Fe}_{100-x}\text{Al}_x$ powders after 35 h of milling time.

Table 1 presents the values of the average crystallite sizes $\langle D \rangle$ (nm) and the mean level of microdistortions $\langle \varepsilon \rangle$ (%) for all samples. It is clear that the crystallite size decreases with increasing Al content from 106 nm for the 0 h (the un-milled sample) to 28 nm for $\text{Fe}_{75}\text{Al}_{25}$ then to 14 nm for $\text{Fe}_{70}\text{Al}_{30}$ and $\text{Fe}_{66}\text{Al}_{34}$. The smallest value of $\langle D \rangle$ (nm) equal to 12 nm was found for the $\text{Fe}_{60}\text{Al}_{40}$ sample. About the mean level of microdistortions, $\langle \varepsilon \rangle$ (%), We note a sharp decreases from 0.49 % for 25 at.% Al to 0.15 % for 30 at.% Al, then $\langle \varepsilon \rangle$ (%) increases again to reach a value of 0.51 % for 40 at.% Al.

Table 1. Average crystallite sizes, $\langle D \rangle$ (nm), and level of microdistortions $\langle \varepsilon \rangle$ (%) versus Al content.

Sample	$\langle D \rangle \pm 1$ (nm)	$\langle \varepsilon \rangle$ (%) ± 0.04
Fe+Al (0 h)	106	0.047
$\text{Fe}_{75}\text{Al}_{25}$	28	0.49
$\text{Fe}_{70}\text{Al}_{30}$	14	0.15
$\text{Fe}_{66}\text{Al}_{34}$	14	0.19
$\text{Fe}_{60}\text{Al}_{40}$	12	0.51

It is interesting to note, for comparison, that the decrease of the average crystallite sizes $\langle D \rangle$ (nm) with Al content ($\text{Fe}_{50}\text{Al}_{50}$, $\text{Fe}_{60}\text{Al}_{40}$ and $\text{Fe}_{70}\text{Al}_{30}$) was observed by E. Jatyč et al. [31] after 800 h of milling using low-energy horizontal ball mill. In this study, the authors found that the $\langle D \rangle$ (nm) values are equal to 7 nm, 5 nm and 4 nm for $\text{Fe}_{70}\text{Al}_{30}$, $\text{Fe}_{60}\text{Al}_{40}$ and $\text{Fe}_{50}\text{Al}_{50}$ respectively. Also, V. Sebastian et al. [29] found a value of $\langle D \rangle$ (nm) equal to 10 nm after 10 h of milling for $\text{Fe}_{100-x}\text{Al}_x$ ($x = 20, 40, 66, 80$ and 90 at %).

3. 2 Microstructure

The powder morphology was studied by SEM. Fig. 3 shows the morphology of Fe and Al (un-milled sample) particles and that of $\text{Fe}_{100-x}\text{Al}_x$ alloy ($x = 25, 30, 34$ and 40 at %) after 35 h of milling.

For the un-milled powder (Fig. 3a), the existence of iron particles (the larger ones) and Al particles (smaller ones) are clearly observed. After 35 h of milling, the micrographs corresponding to the samples with different Al content (Fig. 3b, 3c, 3d and 3e) show the quasi similarity of particles morphology i.e. the presence of particles with different sizes. The majority of particles exhibit a round shape with small diameter; however, one can still note the presence of some big ones having a

platelet shape. We have estimated, from the SEM pictures, the sizes of the particles in the FeAl alloys. A considerable refinement of the particle sizes is observed. After 35 h of milling, the average size value of the particles decreased from 30 μm for 0 h to 5 μm .

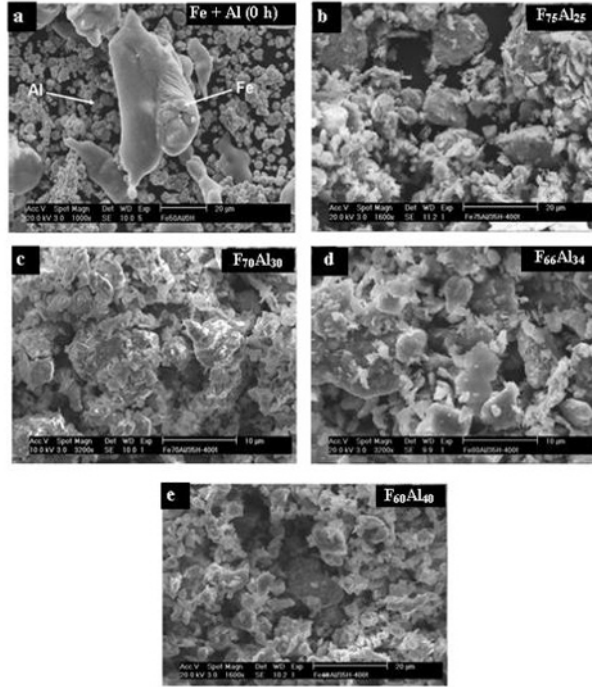


Fig. 3. SEM micrographs of unmilled powder and $\text{Fe}_{100-x}\text{Al}_x$ milled powders for various Al content after 35 h of milling time.

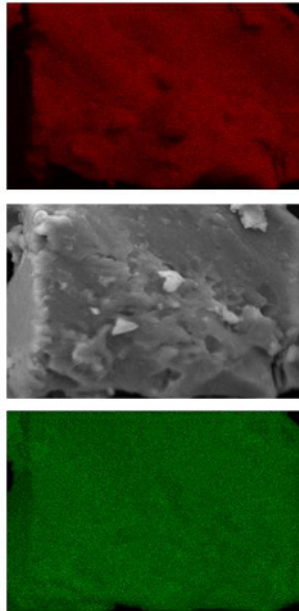


Fig. 4. Maps of Al and Fe distributions for $\text{Fe}_{70}\text{Al}_{30}$ powder milled for 35 h.

Elemental mapping by EDX coupled to the SEM was carried out on the mechanically alloyed powders. Fig. 4 shows an example of the maps of Al and Fe distribution for the selected areas of $\text{Fe}_{70}\text{Al}_{30}$ sample after 35 h of milling. The elemental maps show that the Fe and Al elemental distributions are closely correlated, in the error limits of this method, indicating that the two elements are completely alloyed and the FeAl solid solution is formed. These results are consistent with those obtained from XRD analysis (see section 3.1).

Energy dispersive X-ray (EDX) analyses were made on all samples. Fig.5 shows an example for $\text{Fe}_{70}\text{Al}_{30}$ sample. For all samples, the composition was close to the nominal one and no Cr contamination from the milling media was found in the error limits of this method.

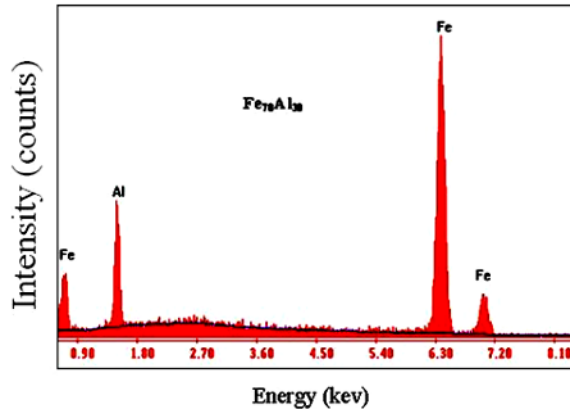
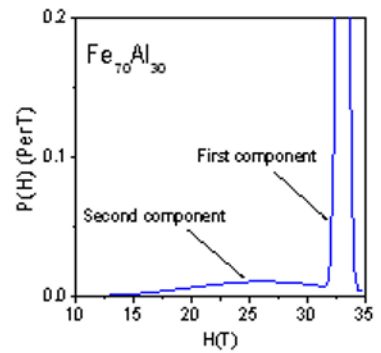
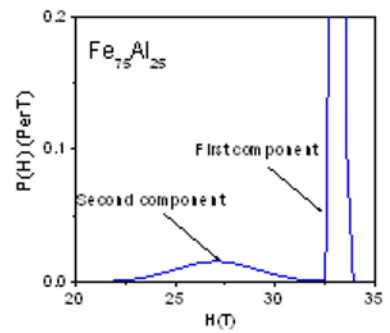
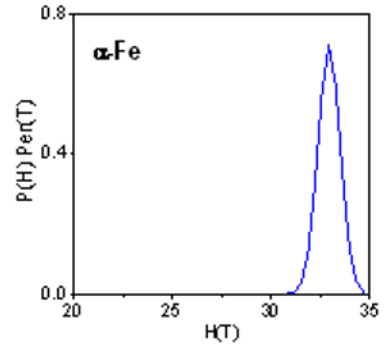
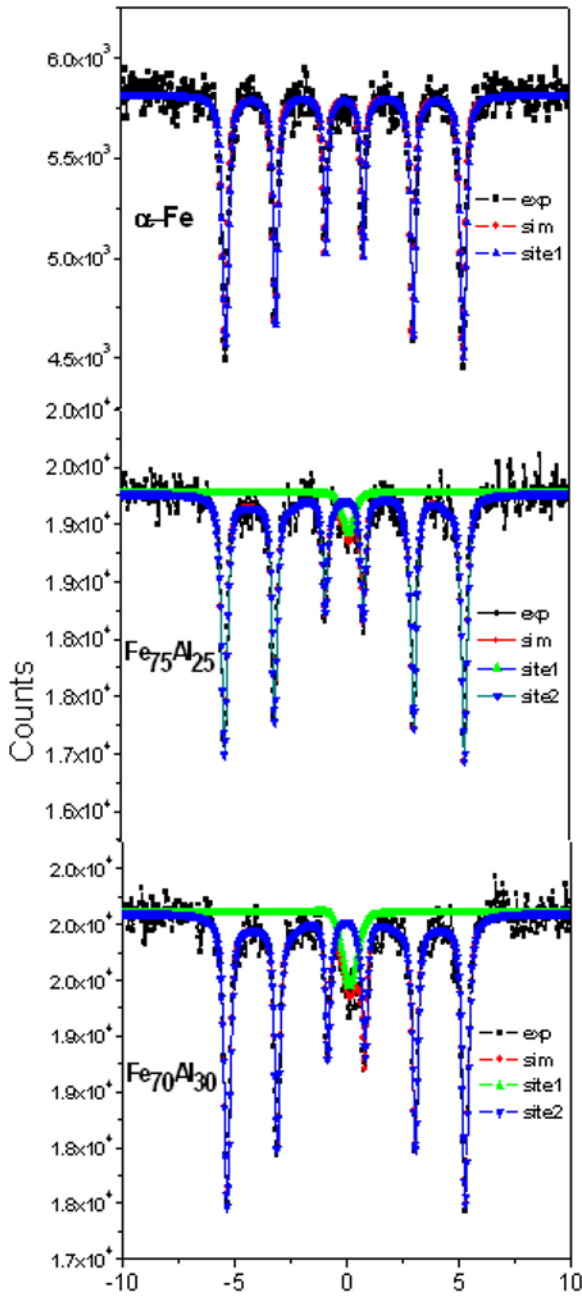


Fig.5. EDX spectrum relative to the $\text{Fe}_{70}\text{Al}_{30}$ powder milled for 35 h.

3. 3 Mössbauer spectroscopy

The Mössbauer measurements were performed in order to monitor the process of alloy formation for each sample. They also enabled us to inspect the local interactions between the iron nuclei as well as to image the nearest neighbourhood of the iron atoms. The room temperature Mössbauer spectra and their corresponding hyperfine field distribution (HFD) for different Al content are shown in Figure 6. For all measured samples, the average values of hyperfine magnetic fields, $\langle H_{\text{hf}} \rangle$ were calculated from distributions. For the un-milled sample, the spectrum shows the presence of a typical sextet with a mean hyperfine field, $\langle H_{\text{hf}} \rangle$, equal to 32.92 T, which corresponds to the α -Fe present in the starting FeAl powder. The full width at half-maximum (FWHM) of the spectral lines was about 0.202 mm s^{-1} .

After milling time of 35 h, the spectra show a broadening of spectral lines in relation to α -iron. The analysis of the spectra show that the full width at half-maximum (FWHM) of the spectral lines increases from 0.202 for 0 h to 0.272, 0.26, 0.29 and 0.24 mm s^{-1} for $\text{Fe}_{75}\text{Al}_{25}$, $\text{Fe}_{70}\text{Al}_{30}$, $\text{Fe}_{66}\text{Al}_{34}$, and $\text{Fe}_{60}\text{Al}_{40}$ respectively. This broadening can be due to the alloying process accompanied with the reduction of the grain size [32-34]. The Mössbauer spectra were fitted with a singlet and one sextet containing two components. The singlet, which increases with increasing Al content, is explained by the formation of a paramagnetic phase characteristic of the A2 disordered structure rich with Al [35, 36]. Concerning the sextet, the first component with a mean hyperfine field values, $\langle H_{\text{hf}} \rangle$ (T) equal to 33.19, 32.96, 32.96 and 32.91 T for $\text{Fe}_{75}\text{Al}_{25}$, $\text{Fe}_{70}\text{Al}_{30}$, $\text{Fe}_{66}\text{Al}_{34}$ and $\text{Fe}_{60}\text{Al}_{40}$, respectively, is attributed to the formation of Fe clusters/ Fe-rich phases [29]. However, for the second component, the obtained $\langle H_{\text{hf}} \rangle$ (T) values equal to 27.17, 26.12, 27.47 and 28.04 T for $\text{Fe}_{75}\text{Al}_{25}$, $\text{Fe}_{70}\text{Al}_{30}$, $\text{Fe}_{66}\text{Al}_{34}$ and $\text{Fe}_{60}\text{Al}_{40}$ respectively, are characteristic of disordered ferromagnetic phases [29, 37].



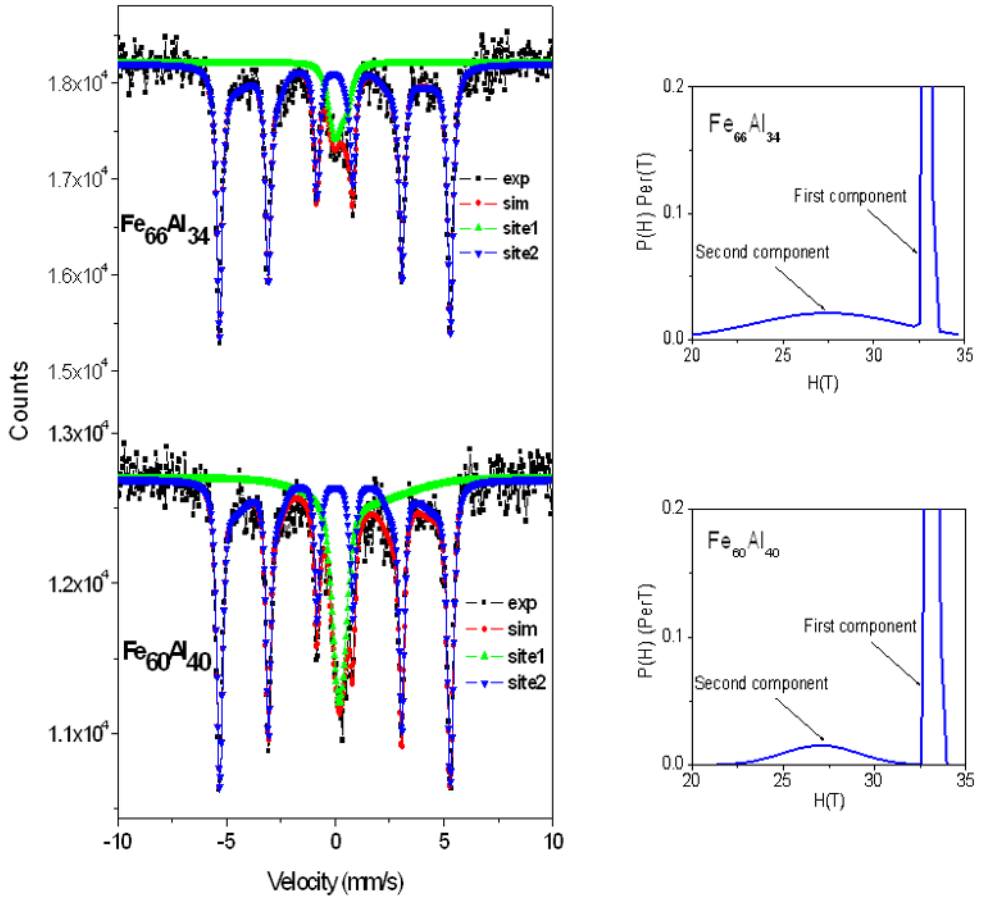


Fig. 6. Mössbauer spectra at room temperature and corresponding relative hyperfine-magnetic field distributions for $\text{Fe}_{100-x}\text{Al}_x$ powders after 35 h of milling time.

A local environment model was applied to estimate the nearest neighbourhood of ^{57}Fe nuclei in FeAl ball milled alloys [38]. According to the data taking from Refs [39, 40], it was assumed that one Al atom in the first coordination sphere decreases the value of hyperfine field by 2.54 T ($\Delta H_1 = -2.54$ T) when at most three aluminium atoms surround ^{57}Fe nuclei and by 4.7 T ($\Delta H_1 = -4.7$ T) when four and more aluminium atoms are located in the nearest neighbourhood. The change of hyperfine field caused by one Al atom in the second coordination sphere was assumed to be 0.89 T ($\Delta H_2 = -0.89$ T). The value $H(m, n)$ of the hyperfine magnetic field at ^{57}Fe site may be described as [31]:

$$H(m, n) = H(0, 0) - m \cdot 2.54 - n \cdot 0.89 \quad (\text{for } m \leq 3) \quad (1)$$

$$H(m, n) = H(0, 0) - m \cdot 4.7 - n \cdot 0.89 \quad (\text{for } m \geq 4) \quad (2)$$

where $H(0, 0)$; denotes the value of hyperfine magnetic field at ^{57}Fe nucleus which is surrounded only by Fe atoms in the first and the second coordination spheres; m the number of impurity atoms in the first sphere; n the number of impurity atoms in the second sphere; ΔH_1 ; ΔH_2 the changes of the hyperfine magnetic field caused by impurity atoms in the first and in the second neighbour shells, respectively.

In our case, the values of average hyperfine magnetic field, related to disordered ferromagnetic phases, are equal to: 27.05, 27.47 and 28.04 T for $\text{Fe}_{75}\text{Al}_{25}$, $\text{Fe}_{66}\text{Al}_{34}$ and $\text{Fe}_{60}\text{Al}_{40}$ respectively. This corresponds to at least two Al atoms in the nearest neighbourhood of the ^{57}Fe atom. For $\text{Fe}_{70}\text{Al}_{30}$

alloy, the average hyperfine magnetic field is equal to 26.12 T; this corresponds to at least three Al atoms in the nearest neighbourhood of the ^{57}Fe atom.

4. Conclusion

From X-ray diffraction spectra we have followed the formation of $\text{Fe}_{100-x}\text{Al}_x$ ($x = 25, 30, 34$ and 40 at %) alloys from elemental Fe and Al powder after 35 h of milling time. It is found that for all the compositions, Al atoms are dissolved into the Fe lattice leading to the formation of bcc Fe(Al) solid solution. This observation is confirmed by EDX elemental mapping. The SEM micrographs taken for different compositions allowed us to follow the morphology of the materials after 35 h of milling. EDX experiments show that for all samples, the composition was close to the nominal one. Increasing Al content leads to an increase of the lattice parameter values and a decrease of the grain size. The Mössbauer spectra were analyzed with a singlet line and a sextet containing two components. The singlet was attributed to the formation of a paramagnetic phase related to the A2 disordered structure rich with Al. For the sextet, the first component was attributed to the formation of Fe clusters/ Fe-rich phases; however, the second component is characteristic of disordered ferromagnetic phase.

References

1. C. Suryanarayana, *Prog. Mater. Sci.*, **46**, 1-184 (2001)
2. S. C. Tjong, H. Chen, *Mater. Sci. Eng.*, **45**, 1-88 (2004)
3. A. Guittoum, A. Layadi, H. Tafat, N. Souami, *J. Magn. Mater.*, **322**, 566- 571 (2010)
4. A. Guittoum, A. Layadi, A. Bourzami, H. Tafat, N. Souami, S. Boutarfaia, D. Lacour, *J. Magn. Mater.*, **320**, 1385-1392 (2008)
5. A. Guittoum, A. Layadi, H. Tafat, A. Bourzami, N. Souami, O. Lenoble, *Philo. Maga*, **88:7**, 1085-1098 (2008)
6. T. Luangvaranunt, T. Threrujirapapong, S. Danchaivijit, K. Kondoh, *J. Solid. Mecha. Mater. Engi.*, **1**, 931-937 (2007)
7. S. Suwas, R. M. Singru, S. Bhargava, *J. Mater. Sci.*, **33**, 109-116 (1998)
8. J. C. wang, D. J. Liu, M. X. Chen, X. X. Cai, *Scrip. Metall. Mater.*, **25**, 2581-2583 (1991)
9. E. P. Elsukov, E. V. Voronina, A. V. Korolev, A. E. Elsukova, S. K. Godovikov, *Phys. Meta. Metall*, **104**, 35-52 (2007)
10. S. Enzo, R. Frattini, G. Mulas, G. Principi, *J. Mater. Sci.*, **39**, 6333-6339 (2004)
11. L. D'Angelo, L. D'Onofrio, G. Gonzalez, *J. Alloys. Comp.*, **483**, 154-158 (2009)
12. M. Sherif El-Eskandarany, *in: Mechanical Alloying for Fabrication of Advanced Engineering Materials*, William Andrew Publishing, Norwich, NY, U.S.A, 2001
13. C. Suryanarayana, *Bull. Mater. Sci.*, **17**, 307- 346 (1994)
14. B. Huang, K. N. Ishihara, P. H. Shingu, *Mater. Sci. Eng.*, **231**, 72-79 (1997)
15. E. Jartych, J. K. Zurawicz, D. Oleszak, M. Pekala, *Nano. Struct. Mater*, **12**, 927-930 (1999)
16. E. Bonetti, G. Scipione, R. Frattini, S. Enzo, L. Schiffini, *J. Appl. Phys.*, **79**, 7537- 7544 (1996)
17. F. Cardellini, V. Contini, R. Gupta, G. Mazzone, A. Montone, A. Perin, G. Principi, *J. Mater. Sci.*, **33**, 2519-2527 (1998)
18. Y. Zou, S. Saji, T. Kusabiraki, *Mater. Res. Bull.* **37**(1), 123 (2002)
19. M. Krasnowski, T. Kulik, *Mater. Chem. Phys.*, **116**, 631-637 (2009)
20. Q. Zeng, I. Baker, *Intermetallics*, **14**, 396-450 (2006)
21. R. H. Fan, J. T. Sun, H. Y. Gong, K. N. Sun, W. M. Wang, *Powd. Tech*, **149**, 121-126 (2005)
22. E. Gaffet, *Mater. Sci. Eng.*, **132**, 181-193 (1991)
23. R. Hamzaoui, S. Guessasma, O. El-Kedim, *J. Alloys Compd.*, **462**, 29-37 (2008)
24. X'Pert High Score software for crystallography, Philips analytical, 2002
25. S. Vives, E. Gaffet, C. Meunier, *Mat. Sci. Eng.*, **A 366**, 229-238 (2004)
26. K. Lagarek, D. Rancourt, Recoil Software, Physics Department, University of Ottawa (1998)

27. L. Castex, J. L. Lebrun, G. Maeder, J. M. Sprauel, *Publs Scient. Tech. ENSAM*, **22**, 51-60 (1981)
28. E. Jartych, J. K. Zurawicz, D. Oleszak, M. Pekala, J. Sarzynski, M. Budzynski, J. Magn. Magn. Mater., **186**, 299-305 (1998)
29. V. Sebastian, N. Lakshmi, K. Venugopalan, *Mater. Lett.*, **61**, 4635-4638 (2007)
30. E. Jartych, J. K. Zurawicz, D. Oleszak, M. Pekala, *J. Phys. Condens. Matter.*, **10**, 4929-4936 (1998)
31. E. Jartych, *J. Magn. Magn. Mater.*, **265**, 176-188 (2003)
32. M. Pekala, D. Oleszak, E. Jartych, J. K. Zurawicz, *Nanostruct. Mater.*, **11**, 789-796 (1999)
33. R. Hamzaoui, O. El-kedim, E. Gaffet, J. M. Greneche, *J. Alloys. Comp.*, **417**, 32-38 (2006)
34. M. Pekala, D. Oleszak, E. Jartych, J. K. Zurawicz, *J. Non-Cryst. Solids*, **250-252**, 757-761 (1999)
35. M. Krasnowski, A. Grabias, T. Kulik, *J. Alloys. Comp.* **424**, 119-127 (2006)
36. D. S. Schmool, E. Araujo, M. M. Amado M. A. Feioa, D. M. Rodriguez, J. S. Garitaonandia, F. Plazaola, *J. Magn. Magn. Mater.*, **272-276**, 1342-1344 (2004)
37. D. Oyola Lozano, Y. Rojas Martinez, H. Bustos, G. A. Pérez Alcazar, *Hyper. Inter.*, **156/157**, 569-574 (2004)
38. I. Vincze, I. A. Campbell, *J. Phys. F.*, **3**, 647 (1973)
39. E. P. Yelsukov, E. V. Voronina, V. A. Barinov, *J. Magn. Magn. Mater.*, **115**, 271-280 (1992)
40. S. M. Dubiel, W. Zinn, *Phys. Rev. B*, **26**, 1574-1589 (1982)